Applied Surface Science 453 (2018) 383–393

Contents lists available at ScienceDirect

Applied Surface Science

journal homepage: www.elsevier.com/locate/apsusc

Full Length Article

Improved biodegradability of Fe–Mn alloy after modification of surface chemistry and topography by a laser ablation

Črtomir Donik[a,*], Aleksandra Kocijan[a], Irena Paulin[a], Matej Hočevar[a], Peter Gregorčič[b], Matjaž Godec[a]

[a] Institute of Metals and Technology, Lepi pot 11, 1000 Ljubljana, Slovenia
[b] Faculty of Mechanical Engineering, Aškerčeva cesta 6, 1000 Ljubljana, Slovenia

ARTICLE INFO

Keywords:
Fe–Mn alloy
Laser ablation
Biodegradability
Surface engineering
XPS depth profiles

ABSTRACT

In this study we report the influence of laser ablation on the controlled biodegradability of a Fe–Mn alloy developed for medical implants. After texturing by a nanosecond Nd:YAG laser, the surface expressed extreme super-hydrophilic wetting properties, since laser ablation led to micro-channels and chemical modification resulting in nanostructured metal oxides. The influence of functionalized surface properties on corrosion behavior was examined on molecular level by using X-ray photoelectron spectroscopy. Results reveal that the oxide layer after the laser texturing of Fe–Mn alloy consists mainly of Fe_2O_3 and FeO, with the content of Mn in the oxide layer being significantly higher than in the bulk. The results of the electrochemical measurements clearly demonstrate the superior biodegradability of the Fe–Mn alloy samples functionalized by laser ablation. Here, the laser-triggered corrosion is self-driven by further production of corrosion products that leads to biodegradability of the whole sample.

1. Introduction

Versatile biodegradable metals for short-term medical implants have been intensively studied in recent years [1–4]. Some of the possible alloys for such applications, especially in orthopaedics (bone-fixation screws, pins, plates, disks), are those based on Fe [5–13]. At the beginning of the healing process, injuries need stable mechanical properties to provide sufficient support. However, as the healing process progresses, the mechanical properties of the implants can be reduced, until finally they are no longer required. Mg- and Zn-based alloys are not suitable for these applications because of their relatively poor mechanical properties, hydrogen evolution and high degradability. On the other hand, stainless steels and Ti-based alloys possess good mechanical properties, but are not intrinsically degradable, which means an additional surgical procedure must be performed for their removal [13–17]. This additional surgical procedure can be avoided by using implants made of tailored, degradable material. One of the possible routes is to add Mn to pure Fe or Fe-based alloys to moderately accelerate the corrosion and consequently make the material suitably degradable. Fe-based biodegradable metals offer a great potential for low, long-term exposure complications, chronic inflammation, side-effect risks or an inability to adapt to the implant [12,15,18–20]. Biodegradable metals are also expected to have a positive interaction during the healing process, and with metals, the degradation process and its products are not supposed to adversely affect the healing process. Fe–Mn-based alloys have suitable characteristics for interactions with human tissue [21,22].

To prepare a metal with a sufficiently high corrosion rate, some authors have added additional elements, such as Si, Pd, C, and S. In this context, many chemical modifications to Fe-based alloys were made during the past few years [5,7,11,15,23–29]. Despite this, just small improvements have been made so far in the enhancement of the biodegradability through chemistry modifications of the alloys. However, a bespoke corrosion rate can also be achieved by modifying the surface topography, which makes it possible to design material properties so as to ensure the correct life span for any particular application. Just recently, surface-roughness modifications, like sandblasting and laser texturing, have been shown to greatly modify the corrosion properties [30–35]. For example, the corrosion is significantly accelerated if the surface wettability after laser texturing is increased [35]. In this case, the interaction between a laser pulse and metal surface modify both, surface topography and its chemistry, since usually metal oxides are formed [36]. Therefore, the main aim of this study is to examine how laser ablation influences the biodegradability properties of an Fe–Mn alloy and to compare these results with different conventional surface treatments like polishing or sandblasting, which also increase the

* Corresponding author.
E-mail address: crtomir.donik@imt.si (Č. Donik).

https://doi.org/10.1016/j.apsusc.2018.05.066
Received 20 March 2018; Accepted 9 May 2018
Available online 17 May 2018

instability of the alloy and the corrosion rate without changing its chemical composition.

The corrosion properties in the current study were investigated using Hank's solution, like the majority of the previous studies that used simulated physiological fluids [10,11,15,37] to simulate in-vivo conditions. Based on previous studies, we used electrochemical impedance spectroscopy (EIS) and potentiodynamic measurements to assess the degradation behavior of the laser-modified Fe–Mn alloy that we investigated. We then analysed the surface modification before and after immersion with a non-contact, optical, three-dimensional system and scanning electron microscopy (SEM). The surface degradation products were analysed and we measured the elemental distribution through the oxide film with an X-ray photoelectron spectroscopy (XPS).

2. Material and methods

2.1. Material preparation

Material Preparation – the investigated Fe-based alloy with 18 wt% Mn (Fe–Mn) was custom produced from pure Fe with the addition of Mn to the alloy. Both materials were melted in an induction furnace under an air atmosphere at approximately 1700 °C and cast into an iron mould. The cast Fe–Mn was hot rolled at approximately 1000 °C for a 33 % reduction. The literature [18,19,38] suggests that hot-rolled material without being annealed and/or homogenized has a higher corrosion rate. The chemical compositions of the alloy, revealed in Table 1, was determined using an X-ray fluorescence (XRF) spectrometer (Thermo Scientific Niton XL3t GOLDD +) and using a carbon and sulphur analyser (ELTRA CS-800).

2.2. Surface treatments

Surface treatments – pure Fe and some Fe–Mn samples were prepared by grinding down to 1200 grit and polishing down to 1 μm with a diamond suspension. The selected Fe–Mn samples were additionally processed by laser texturing. Here, a Nd:YAG (λ = 1064 nm) pulsed laser with a pulse duration of 95 ns (full width at half maximum) was used. The laser beam was focused on the surface by an F-theta lens with a focal distance of 160 mm. Since the surface was placed in the focal position, the beam spot size equalled 0.05 mm and it was led in lines with a velocity of 1.6 mm/s using a 2D scanner. For the processing, we used a 1-kHz pulse frequency and 0.6 W of average power, resulting in pulses with an energy of 0.6 mJ and spots separated by 1.6 μm, forming a channel. The distance between two adjacent lines, i.e., the scan line separation, was set to 50 μm.

2.3. X-ray photoelectron spectroscopy (XPS)

X-ray photoelectron spectroscopy (XPS) depth profiles of the oxide layers were measured with a VG Microlab 310F SEM/AES/XPS. For all the XPS measurements Mg-K_α radiation at 1253.6 eV with an anode voltage × emission current 12.5 kV × 16 mA = 200 W power was used. For the investigation of the elemental composition with depth, Ar^+ ions with an energy of 3 keV at 1 μA ion were applied over the area of 4 × 4 mm^2. Similar ion-beam parameters were used for sputter-cleaning the sample, except that the raster area was closer to 10 × 10 mm^2 in this case. No exact calibration is available for this material, but a rough estimate for the sputtering rate at these profiling parameters is of the order of 0.01 nm/s, which is consistent with some calibration measurements performed on metallic and oxide-type samples as well as with some reference data for the sputtering rates for Fe and its oxides. The ratio of our corrosion product (Fe_2O_3) and SiO_2 is 0.61 in the literature [39]. We used sample rotation during the depth profiling, since it is important to avoid shadowing for proper XPS depth profiling [40]. The spectra were acquired using Avantage® 3.41v data-acquisition & data-processing software supplied by the AES/XPS equipment manufacturer. Ar^+ sputtering for different time intervals estimated the thickness of the oxide layer. Casa XPS® software (http://www.casaxps.com) was used for the detailed data processing.

Table 1
Chemical composition of used materials in wt%.

Material	Mo	Mn	Cu	Ti	Si	C	Fe
pure Fe	< LOD	0.262	0.043	< LOD	0.051	0.19	Balance
Fe–Mn alloy	0.31	18.0	0.051	0.058	0.067	0.58	Balance

2.4. Scanning electron microscopy (SEM)

Scanning Electron Microscopy (SEM) analyses using a FE-SEM JEOL JSM-6500F were employed to investigate the morphology of the different Fe–Mn surfaces as well as the morphology and distribution of the corrosion products after a corrosion evaluation.

The surface topographies of the polished and laser-textured samples prior to and after the corrosion experiments were examined with a non-contact, optical, three-dimensional Alicona G4 InfiniteFocus (IF) system (Alicona Imaging GmbH, Graz, Austria). The 3D surface-roughness parameters, including the average height of the selected area (S_a), were obtained and calculated from the Alicona InfiniteFocus images using IF-MeasureSuite® 5.1 software.

2.5. Electrochemical measurements

Electrochemical measurements were performed on prepared specimens, ground with SiC emery paper down to 1200 grit and polished down to 1 μm with a diamond suspension. The laser-textured samples had no previous preparation other than the laser modification. The experiments were carried out at room temperature in a simulated physiological Hanks solution, containing 8 g/L NaCl, 0.40 g/L KCl, 0.35 g/L $NaHCO_3$, 0.25 g/L $NaH_2PO_4{\cdot}2H_2O$, 0.06 g/L $Na_2HPO_4{\cdot}2H_2O$, 0.19 g/L $CaCl_2{\cdot}2H_2O$, 0.41 g/L $MgCl_2{\cdot}6H_2O$, 0.06 g/L $MgSO_4{\cdot}7H_2O$ and 1 g/L glucose, stabilized at pH = 7.8. All the chemicals were from Merck, Darmstadt, Germany. The measurements were performed using a three-electrode, flat BioLogic® corrosion cell (volume 0.25 L). The test specimen was employed as the working electrode (WE). The reference electrode (RE) was a saturated calomel electrode (SCE, 0.242 V vs. SHE) and the counter electrode (CE) was a platinum mesh. Electrochemical measurements were recorded using a BioLogic® Modular Research Grade Potentiostat/Galvanostat/FRA Model SP-300 with an EC-Lab® software V11.10. The specimens were immersed in the solution 1 h prior to the measurement in order to stabilize the surface at the open-circuit potential (OCP). *The potentiodynamic curves* were recorded after 1 h of sample stabilization at the open-circuit potential (OCP), starting the measurement at 250 mV vs. SCE more negative than the OCP. The potential was then increased, using a scan rate of 1 mV/s. Long-term open-circuit *electrochemical impedance spectra* (EIS) were obtained for the investigated samples at the OCP, with a sinus amplitude of 10 mV peak-to-peak and a frequency range of 65 kHz to 1 mHz, directly after immersion for 1 h, 3 h, 6 h, 12 h, 24 h, 48 h and 72 h. All the measurements were made at room temperature and were repeated at least three times. The impedance data are presented in terms of Nyquist plots and Bode-Bode plots. For the fitting process Zview® v3.5b Scribner Associates software was used.

3. Results and discussion

3.1. XPS measurements

XPS analyses with depth profiles were acquired by fitting the spectra, as shown in Fig. 1. Narrow-range XPS scans show Fe $2p_{3/2}$ and Mn $2p_{3/2}$ transitions with the corresponding metallic and oxide

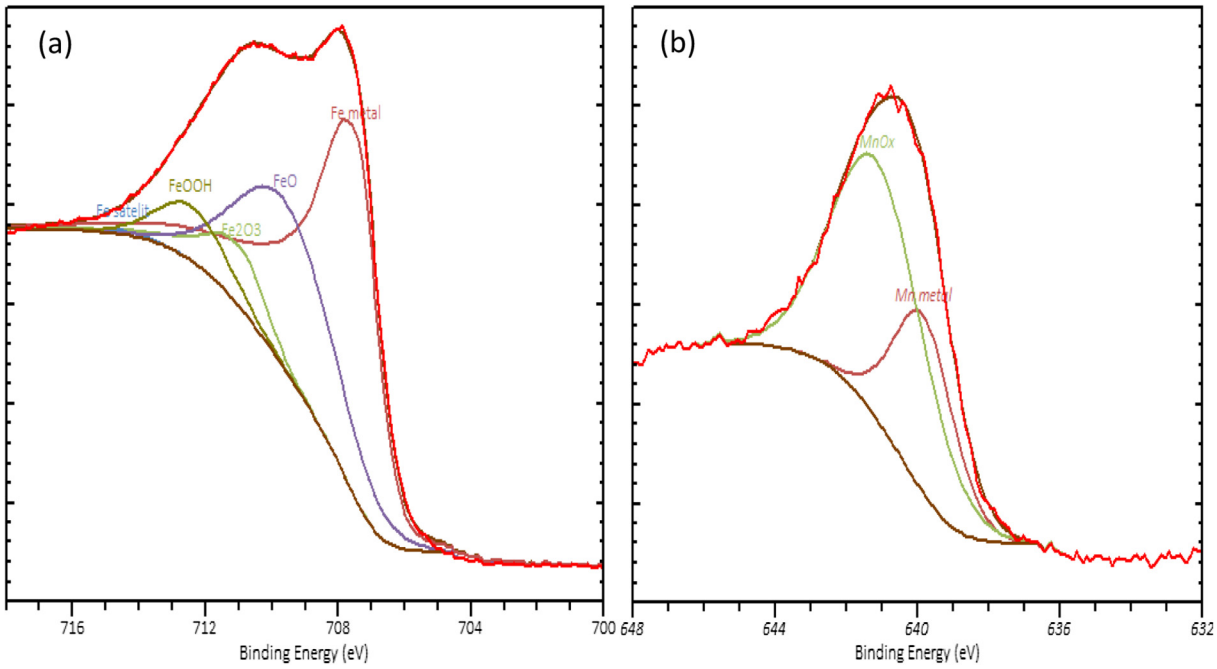

Fig. 1. Examples of fitted (a) Fe $2p_{3/2}$ and (b) Mn $2p_{3/2}$ XPS spectra.

components. The Fe $2p_{3/2}$ peak, from the as-received surface of the pure Fe, was measured at binding energies of 700 eV and 720 eV. The Fe $2p_{3/2}$ spectra are curve fitted in Fig. 1(a) using Fe_2O_3 at 710–711 eV, the hydrated oxide FeOOH at 711.5 eV, FeO at 709.6 eV and Fe metal at 707.5 eV, together with the O 1s peaks for FeO_x at 529.7 eV [41–44]. For the C1s fitting we used 284.7 eV for the hydrocarbon and 286.0 eV for the C-O [45,46]. The Mn $2p_{3/2}$ peak from the polished surface of the Fe–Mn alloy sample was measured at binding energies of 630 eV and 645 eV. The Mn $2p_{3/2}$ spectra are curve fitted in Fig. 1(b). The Mn oxides Mn_2O_3, MnO_2, Mn_3O_4 and other, (MnO_x in the spectra) are combined together, while the differences in energies in the XPS spectra are in the range of a few tenth of eV and are not far enough apart to differentiate in the XPS spectra. The MnO_x peaks are at 641–643 eV, while the Mn metal is at 639.5 eV [44,47].

The XPS composition depth profiling was made for different lengths of sputtering time, with a rough estimation for the sputtering rate of the order of 0.01 nm/s. XPS depth profiles of the relative concentration of the metallic and oxide species are presented in Figs. 2–4. Here, after each sputtering the composition of each oxide and metallic species was plotted cumulatively, with the total composition summed to 100 at%.

Fig. 2 reveals the composition of the Fe and its oxides on the polished pure Fe and the same sample after 3 days immersed in Hank's solution. The oxide on the surface of the polished Fe (Fig. 2a) does not possess the properties of a "protective layer" and its thickness is very narrow. After the first sputtering (600 s), Fe as a metal is present in the amount of 80 at%, while the oxides present around 15 at%. After the second stage of the Ar-ion etching (1200 s), the composition consists of just Fe metal and remains in the same range until the end of the measured depth profile. The native oxides present on the surface are FeO and Fe_2O_3; also Fe in metal form is visible in the first spectra, so this oxide layer is thinner than 3 λ allowing to calculate the thickness by using Compton's method – Thickogram (Eq. (1)) [48,49].

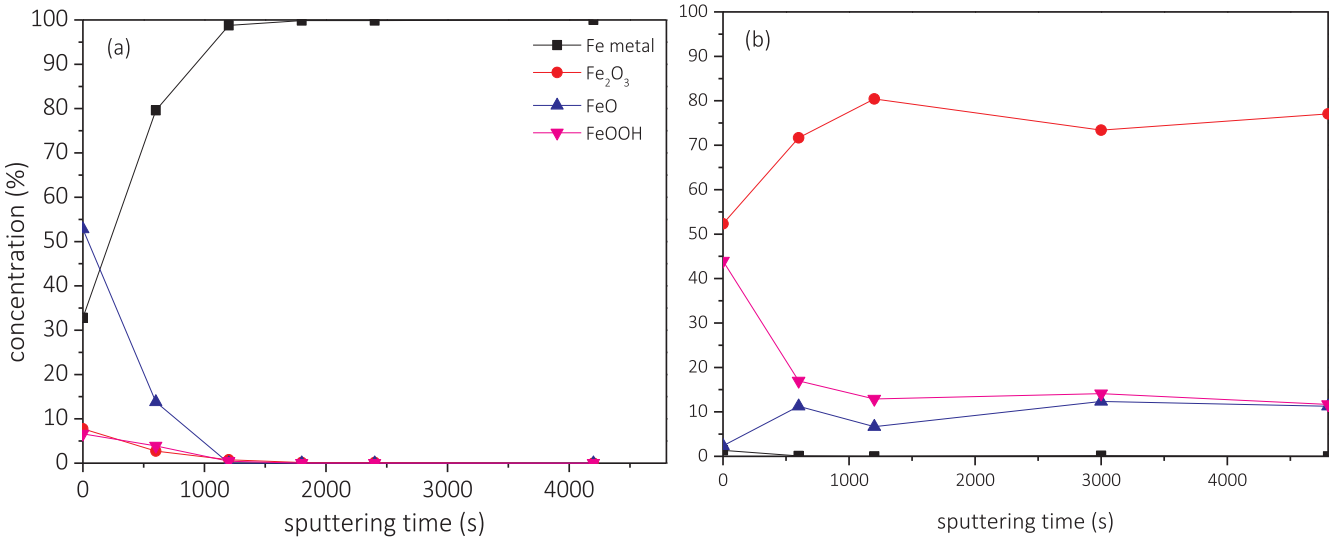

Fig. 2. XPS depth profile of pure Fe (a) before and (b) after 3 days of immersion in Hank's solution. The concentration is shown in at%.

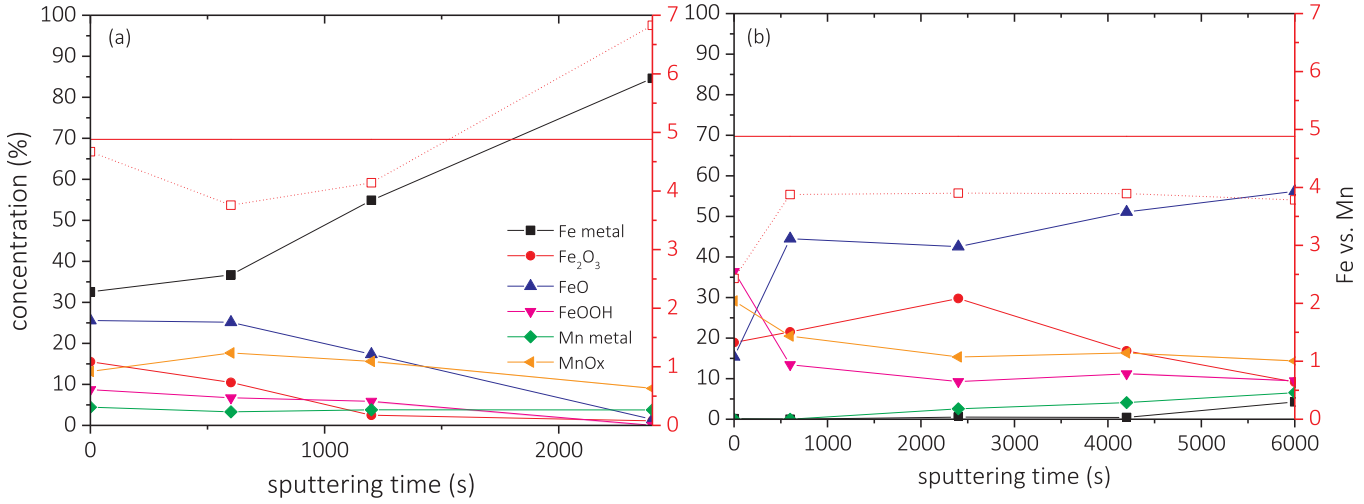

Fig. 3. XPS depth profile of (a) polished Fe–Mn and (b) the same sample after 3 days of immersion in Hank's solution. The Fe/Mn ratio is shown on the second Y-axis. The solid red line shows the Fe/Mn ratio for the bulk material, while the red dotted line shows the same ratio throughout the oxide layer. The concentration is shown in at%. (For interpretation of the references to colour in this figure legend, the reader is referred to the web version of this article.)

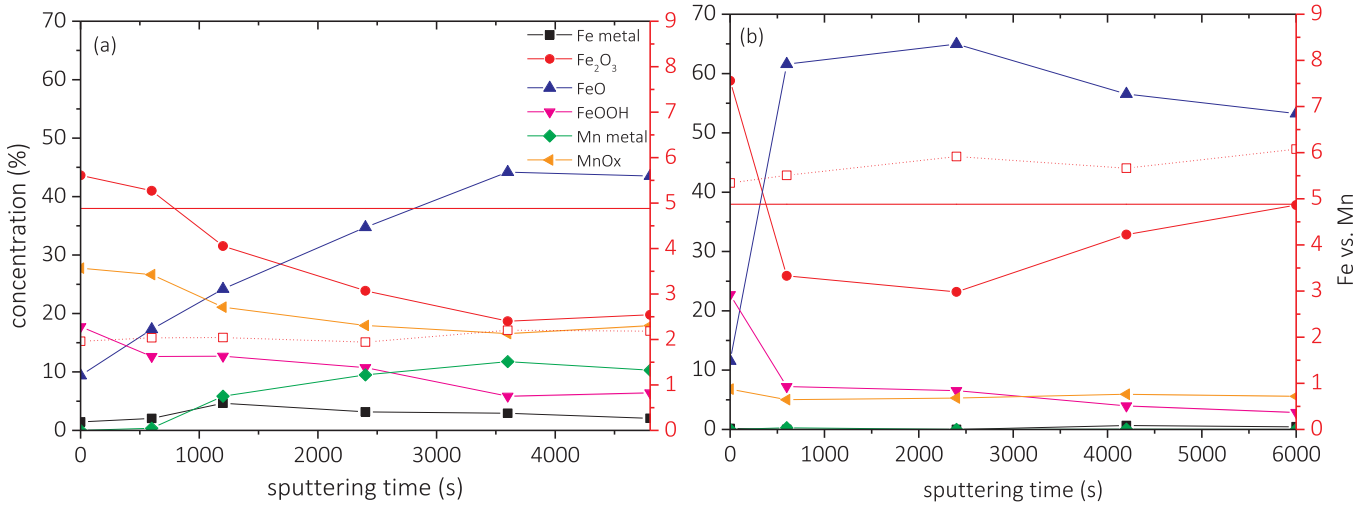

Fig. 4. XPS depth profile of (a) laser-textured Fe–Mn and (b) laser-textured Fe–Mn after 3 days immersion in Hank's solution. The Fe/Mn ratio is shown on the second Y-axis. The solid red line shows the Fe/Mn ratio for the bulk material, while the red dotted line shows the same ratio throughout the oxide layer. The concentration is shown in at%. (For interpretation of the references to colour in this figure legend, the reader is referred to the web version of this article.)

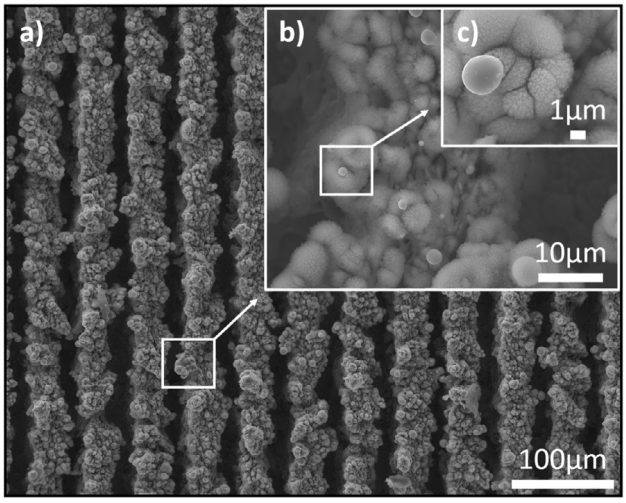

Fig. 5. SEM image of surface topography of Fe–Mn laser-textured sample.

$$d = -\lambda \cos\theta \ln\left(1 + \frac{I_o}{I_s}\right) \quad (1)$$

where d stands for the film thickness, λ is the attenuation length of the metal photoelectrons in the (oxide) layer, θ represents the emission angle (measured with respect to the surface normal), while I_o and I_s are the measured peak intensities from the layer and the substrate, respectively. In our equipment, the emission angle θ relative to the detector is 90°. From the measured data, the thickness of the native surface oxides on the polished pure Fe is in the range of 1.3 λ and with the known attenuation length of Fe, approximately equals to 1.5 nm [48].

Fig. 2b shows the depth profile of the same sample after 3 days of immersion in Hank's solution. The surface oxide composition is significantly different in comparison by the one on the polished Fe sample. The Fe in metal form is not present anymore even for a prolonged sputtering times. Which proves the fact that corrosion of pure Fe does not passivate and these oxides accelerate the corrosion.

Fig. 2 clearly demonstrates how corrosion advances on pure Fe. When corrosion starts, the Fe in metal form disappears, and the different Fe oxides are formed which contribute in further autocatalytic corrosion on non-passivated steels [50]. Therefore, the thickness of the

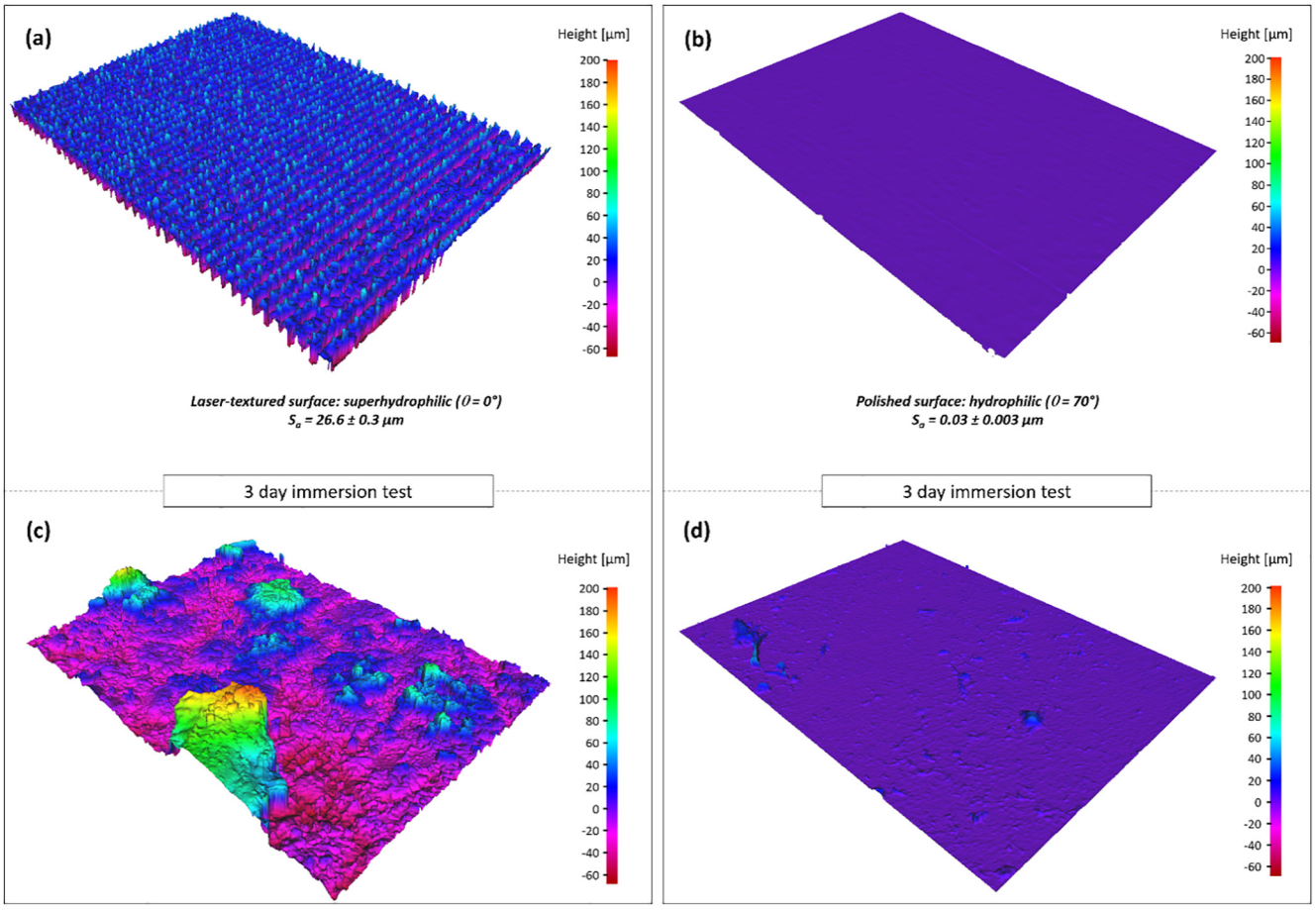

Fig. 6. 3D height image representing the surface topography of (a) and (c) laser-textured Fe–Mn sample before and after 3 days of immersion; (b) and (d) polished Fe–Mn sample before and after 3 days of immersion.

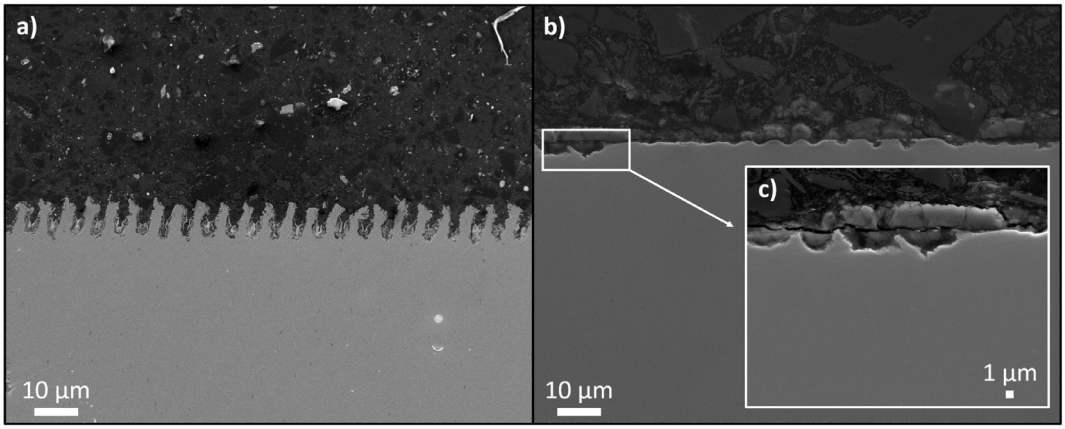

Fig. 7. SEM images of surface topography of (a) Fe–Mn laser-textured sample, (b) and (c) after 3 days of immersion.

oxidized layer is significantly larger and unfortunately cannot be measured with Compton's Thickogram for the comparison with previous two measurements. The arrangement of the Fe oxides is as follows: the main component is Fe_2O_3 with around 80 at% of the oxide layer, followed by 10–15 at% of interchangeable FeO and FeOOH throughout the layer.

Figs. 3 and 4 reveal the XPS compositional depth profiles of the polished and laser-textured Fe–Mn alloys, respectively (before and after immersion in Hank's solution for 3 days). Mn is added to Fe-alloys in order to achieve the appropriate degradation times, since it is the most appropriate alloying element from the point of view of microstructural, corrosion, magnetic and toxicological properties. In Fe–Mn alloys, the Fe/Mn ratio, defined as the ratio between Fe and Mn concentrations on surfaces, is an important measure that correlates with the corrosion rate. Lower Fe/Mn ratios (i.e., the increased concentrations of Mn on the surface) lead to increased corrosion rates. Therefore, the second Y-axis (red axis, on right-hand side) was included in Figs. 3 and 4 to present the Fe/Mn ratio, with the original bulk Fe vs. Mn ratio of 4.88 (the solid red line).

The red dotted line with empty squares reveals the Fe/Mn ratio throughout the oxide layer, calculated from the sum of all the Fe and Mn peak areas. The XPS composition depth profile of the polished

Table 2
Corrosion characteristics of studied materials calculated from potentiodynamic measurements.

	I_{corr}/μA	E_{corr}/mV	v_{corr}/ nm year^{-1}	R_p/Ω	A_S/A_R ratio before corrosion tests	A_S/A_R ratio after corrosion tests
Fe	5.4	−735	62	2 623	1.0	1.02
Fe–Mn laser	73.6	−755	863	410	4.2	1.5
Fe–Mn polished	10.4	−699	121	869	1.0	1.03

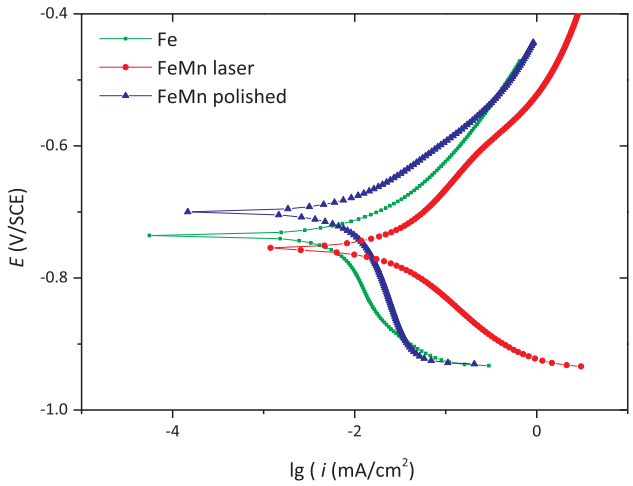

Fig. 8. Potentiodynamic curves of Fe, Fe–Mn polished and Fe–Mn laser textured.

Fe–Mn alloy is presented in Fig. 3a. The main constituent of the top surface layer is Fe metal, around 33 at%, and Mn metal, around 5 at%. This demonstrates the thinness of the oxide layer, similar to the polished pure Fe. The thickness of the oxide layer on the top surface, calculated with Thickogram (Eq. (1)), is around 2.3 nm and is, as expected, a little thicker than the polished pure Fe. The main oxide here is FeO (25 at%), followed by Fe_2O_3 (15 at%), FeOOH (a little below 10 at %), with MnOx (around 15 at%). The oxide layer is a little thicker, which corroborates with the slightly increased corrosion properties obtained with the electrochemical measurements. As expected, the composition alters through the oxide layer and shifts towards the Fe metal, while the other detected species are just interchanging and none of the species exceed more than 10 at%. After 2400 s of sputtering the detected amount of Fe is around 85 at%, the Mn is around 10 at%, while the rest are oxides, comprising less than 5 at%. An interesting feature can be observed with the Fe/Mn ratio throughout the layer. On the top, the ratio is as designed for this alloy, whereas with the sputtering, the Fe/Mn ratio decreases in favour of Mn, while after 2400 s of sputtering, the ratio is a little in favour of Fe. These ratios show that just polished Fe–Mn does not significantly improve corrosion due to the native surface oxides. Nevertheless, the ratio in the Fe–Mn polished sample is in the range close to the originally designed ratio.

Fig. 3b shows the Fe–Mn polished sample immersed in Hank's solution for 3 days. It indicates FeOOH as the main oxide on the surface (about 35 at%), followed by Mn oxides, MnOx (almost 30 at%) and FeO and Fe_2O_3 (both around 20 at%). With the exposure to Hank's solution the following interesting occurrence was observed: the Fe/Mn ratio on the top-most layer is around 2, i.e., strongly in favour of Mn. This confirms that the first element that dissolves in the solution and reacts in corrosion processes is Fe. Therefore, without any additional initiation, the corrosion mechanism of the investigated Fe–Mn alloy acts equally as the pure Fe and the corrosion is not altered significantly, which was confirmed by the corrosion results where the polished pure Fe and Fe–Mn act alike.

The surface chemical composition of the laser-textured Fe–Mn alloy before and after exposure to Hank's solution is presented in Fig. 4. It is clearly visible in Fig. 4a that laser texturing significantly influences surface chemistry since it transfers the majority of the Fe into corrosion favourable Fe oxides. As visible from Fig. 4a, Fe_2O_3 is the main oxide with concentration up to 45 at% in the oxide layer, followed by MnOx (around 27 at%), FeOOH (a little below 18 at%) and FeO (around 9 at %). By sputtering the concentration of all the Fe oxides decreases, except FeO, which is increased, at the end to approximately 45 at%. The interesting feature of laser texturing is the Fe and Mn in metal form. This is most probably related to the micro splashing of the metal drops during the laser texturing and some parts of the metal stay exposed without the thick oxide layer. These exposed small droplets were also observed on the SEM images (Fig. 5) and they even play an additional role in increasing the corrosion rate. The Fe/Mn ratio is another interesting property of the laser-treated sample. The laser-treated sample before corrosion measurements has the Fe/Mn ratio of around 2; this means that the overall concentration of Fe on the surface is much decreased compared to the bulk with very small amount of Fe metal. The concentration of the Mn metal is increasing in the layer while the Fe/Mn ratio does not change throughout the observed oxide layer. The laser-textured Fe–Mn sample with corresponding Fe/Mn ratio, much in favour of Mn, shows also increased corrosion rate [20]. With this surface treatment the chemical composition of the top most oxides show much less corrosion resistance compared to polished Fe–Mn with same chemical composition.

Fig. 4b presents as the main oxide on the surface Fe_2O_3 with concentration of almost 60 at% of the oxide layer, and it switches after the first sputtering with FeO, which jumps from 12 at% to more than 60 at %. The third oxide is FeOOH, at the surface around 23 at%, and after the sputtering its concentration drops to around 5 at%. Mn, like Fe, is present just in oxide form and as the ratio is around 6, just approximately 5 at% of the oxide layer. The presence of metallic species is not possible due to the high corrosion rate and the corrosion products on the surface (Fig. 6).

Regardless of the oxide layer's composition the Fe/Mn ratio dramatically changes to almost 6 after the exposure to Hank's solution, as visible in Fig. 4b. The main reason for this increase in favour of Fe is due to the low corrosion stability of Mn and its oxidises which degrade in the process of corrosion. Nevertheless, the concentration of the Mn is decreased and the ratio is close to the ratio in the bulk material, the corrosion rate, after three days of exposure in Hank's solution, is even increased in comparison to the sample of as received sample. This reveals the complexity of the corrosion process which in our case involves the surface roughness with increased wettability and surface area, chemistry of the bulk material, the high-temperature oxides after laser ablation and at the end also the corrosion products which form after the sample is exposed to corrosive media. This corroborates with our assumption that the laser texturing and increased area with oxides on the surface will increase the corrosion even after the "texturing" is removed and with known "self-driven" corrosion mechanism, so the whole sample will degrade in desired rate.

3.2. Surface topography

The modification of surface morphology after laser texturing is shown by SEM image on Fig. 5. It is clearly visible that micro-channels separated by 50 μm are formed due to the laser ablation. At the top of these micro-channels a bimodal structure with a typical dimension of 10 μm is formed. This bimodal surface is covered by a nanostructured oxide. The surface topography was evaluated by 3D measurements using an optical microscopy and is presented in Fig. 6. Fig. 6a reveals that the micro-channels are 120 μm deep. For comparison, a 3D profile

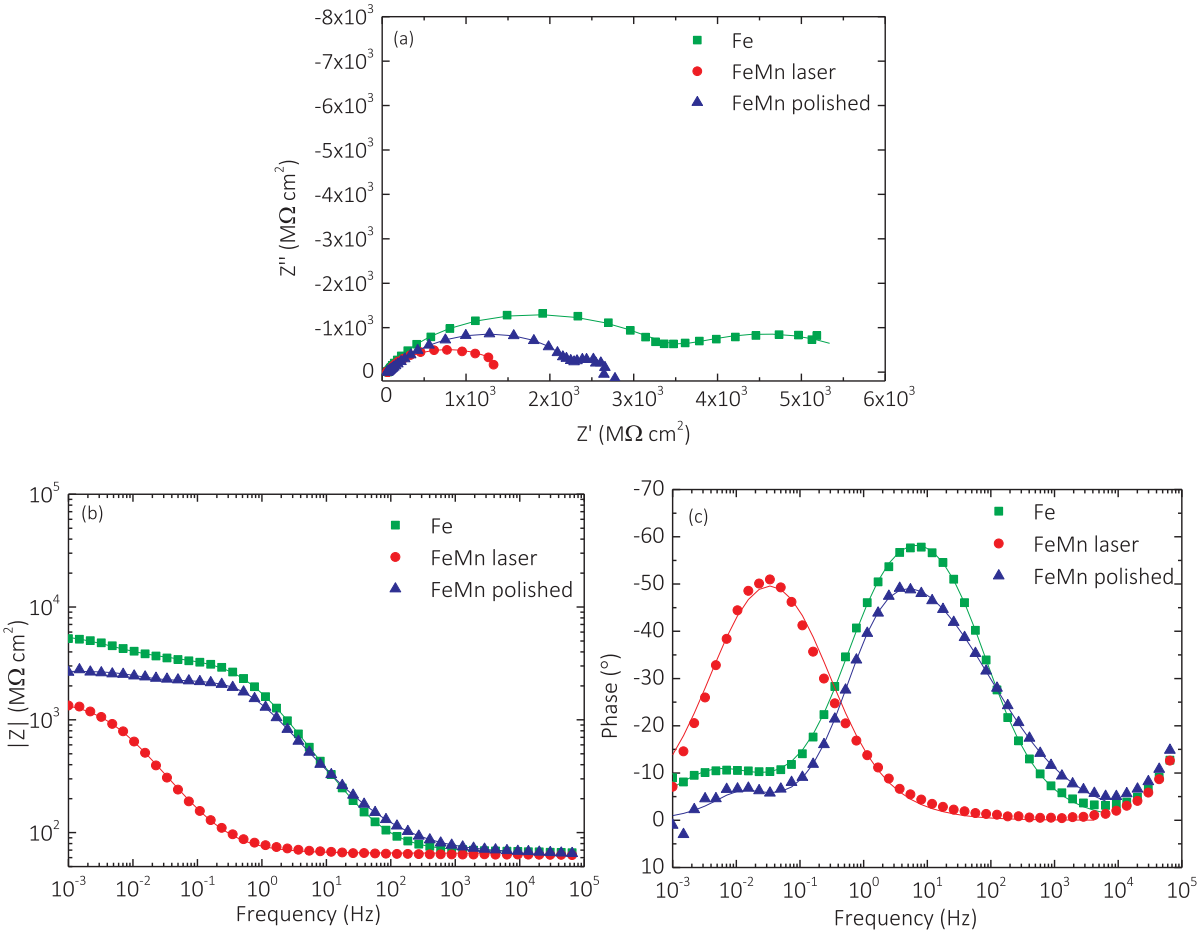

Fig. 9. EIS spectra (a) Nyquist, (b) and (c) Bode–Bode diagrams for Fe, Fe–Mn polished and Fe–Mn laser-textured samples after immersion in Hank's solution for 1 h.

of the polished (reference) surface is shown in Fig. 6b. These results lead to conclusion that laser ablation significantly influences surface topography in sense of increased surface roughness.

The rough-surface area was measured with Alicona Imaging system and the ratio A_0/A_R between the area of the smooth surface, A_0 (defined as a product of width and height of the processed area), and the area of the rough surface A_R, was estimated. For the polished surface this ratio equals $A_0/A_R = 1$ and it is increased due to laser ablation (after laser texturing and before the corrosion measurements) to $A_0/A_R = 4.2$. However, after the 3-days of corrosion tests this ratio decreases to $A_0/A_R = 1.5$, since the micro-topography induced by a laser ablation was removed from the samples' surface due to corrosion (Fig. 7).

The impact of the corrosion attack on the surface topography after 3 days of immersion in Hank's solution is shown in Fig. 6c for the laser modified surface, while Fig. 6d shows the same for the reference, polished surface. The laser-textured sample is fully covered by corrosion products, so the texturing effect is not visible on the surface topography anymore. These corrosion products are different Fe oxides (Fig. 4b) and leads to self-driven corrosion of the whole sample. On the contrary, the polished sample shows just little islands of the corrosion products on the surface and its A_0/A_R ratio stays around 1.03 also after corrosion tests (see also Table 2). Therefore, it can be concluded that the laser texturing is an important trigger for enhanced and self-driven corrosion of the processed material.

3.3. Surface wettability

As already known and explained by several authors [35,36,51,52], the surface texturing influences also surface wettability. Static-contact-angle measurements performed immediately after laser texturing showed that our surface was super-hydrophilic in a saturated Wenzel regime [53] with a static contact angle of $\theta = 0^\circ$. This means that a water droplet that was placed on the surface spilled into a thin film covering the whole surface. As previously shown [35], the corrosion rate for such a surface is significantly increased. The static contact angle was measured again after keeping the sample into atmospheric air for 6 months (just before the electrochemical test were performed) and the sample was still super-hydrophilic with a static contact angle of $\theta = 0^\circ$. As a reference, the static contact angle, measured with a 5 μL water droplet on the polished surface, equals $\theta = 70^\circ$ and it was also constant by time.

3.4. Electrochemical measurements

3.4.1. Potentiodynamic measurements

Potentiodynamic curves of the Fe, polished Fe–Mn and laser-textured Fe–Mn alloy in a simulated physiological Hank's solution at pH = 7.8 are presented in Fig. 8. After 1 h of stabilization at the OCP, the corrosion potential (E_{corr}) for pure Fe in Hank's solution was approximately −0.735 V vs. SCE. The polished Fe–Mn alloy exhibited similar potentiodynamic behavior as the pure Fe, with E_{corr} at approximately −0.7 V vs. SCE. In the case of the laser-textured Fe–Mn sample the corrosion stability decreased compared to the other two samples, the Tafel region has been shifted to higher corrosion-current densities and E_{corr} was approximately −0.755 V vs. SCE. The corrosion parameters calculated from the potentiodynamic measurements indicated the highest corrosion stability of Fe, followed by the polished Fe–Mn alloy and the lowest corrosion stability of the laser-textured Fe–Mn sample. The superior degradability of the laser-textured Fe–Mn alloy under the biological conditions was proven in terms of a higher

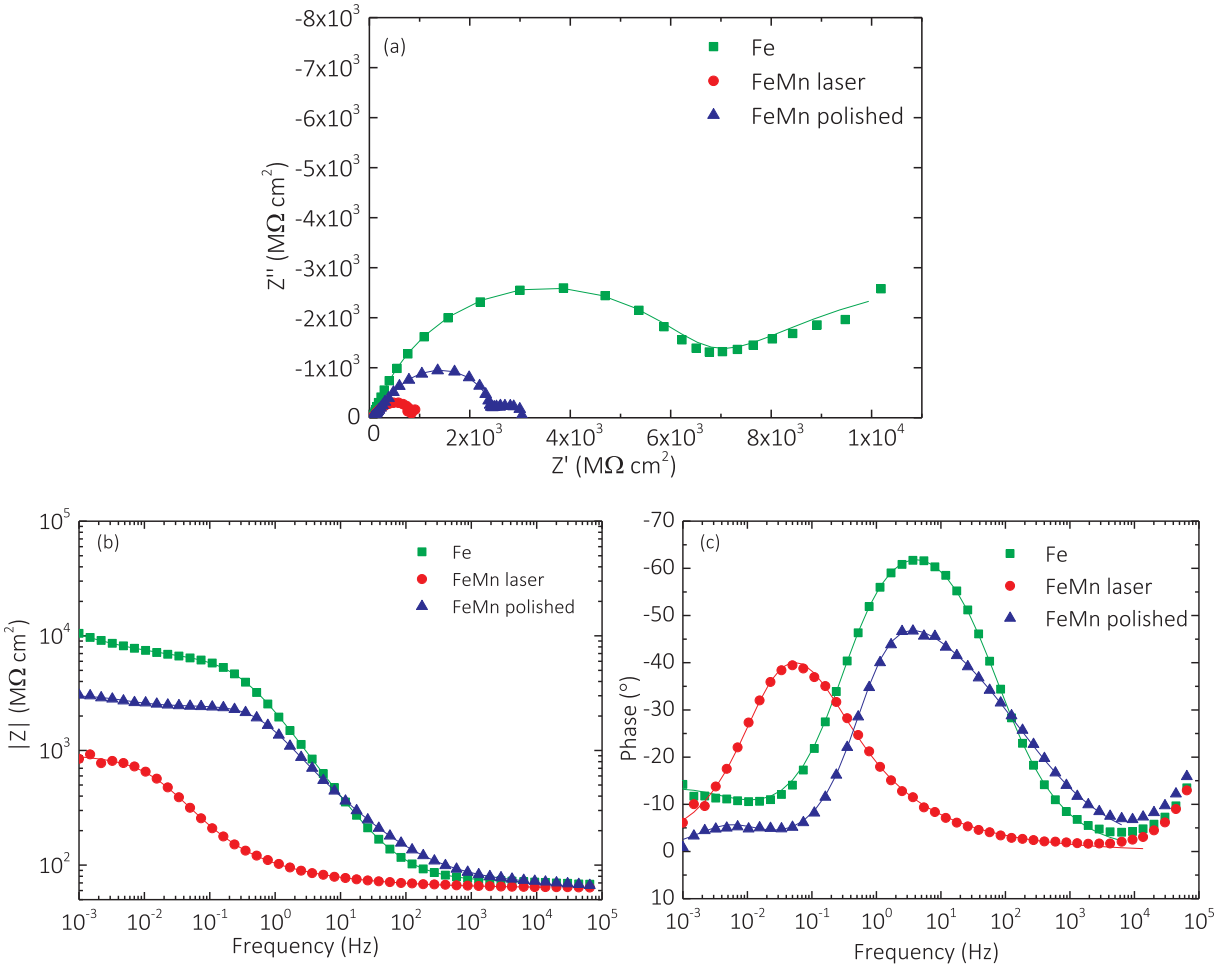

Fig. 10. EIS spectra (a) Nyquist, (b) and (c) Bode–Bode diagrams for Fe, Fe–Mn polished and Fe–Mn laser-textured samples after immersion in Hank's solution for 1 day.

corrosion current (I_{corr}), a higher corrosion rate (v_{corr}) and the lowest polarization resistance (R_p), compared to polished Fe–Mn and Fe samples (Table 2).

The presented corrosion measurements show 13-times and 7-times increase in corrosion rate of the laser-textured surfaces in comparison to the polished Fe and Fe–Mn surfaces, respectively. This is significantly higher as 4.2 times increased surface area due to the laser ablation. The increased corrosion activity after the laser texturing is a result of super-hydrophilic state leading to better penetration and degradation on the surface. Here, an important role play also the chemical modification of surface due to the laser-induced high-temperature oxides. However, the corrosion activity stays increased also after the roughness of the corroded surface is reduced by 3 times to $A_S/A_R = 1.5$. This corroborates to the well-known fact that porous iron oxides accelerate the corrosion even more than high-temperature oxides formed after laser-texturing [50]. The presented results, therefore, additionally prove that laser texturing triggers the increased corrosion of the developed Fe–Mn alloy and that the corrosion is self-driven also after the functionalized surface is already removed. This opens important ability to use the proposed laser-texturing method as a tool for further development of new types of biodegradable materials.

3.4.2. Electrochemical impedance spectroscopy measurements

The corrosion performance of the polished and laser-textured Fe–Mn samples was additionally studied by EIS. The open-circuit impedance spectra of the investigated samples were measured over a 3-days immersion period in the simulated physiological Hank's solution. Figs. 9–11 show the EIS Nyquist and Bode plots for all the investigated samples after 1 h, 1 day and 3 days of immersion in Hank's solution, respectively. The results for Fe under the same conditions were used for a comparison.

In the case of the laser-textured Fe–Mn sample after the initial immersion period, the spectra were characterized by one time constant corresponding to the charge-transfer process (Figs. 9 and 12a). After the initial immersion stage, the spectra displayed two time constants attributed to the oxide-film formation and the charge-transfer process (Figs. 9 and 10). The equivalent circuit that was used to fit the experimental data considered (i) the solution resistance R_s; (ii) the charge-transfer resistance R_{ct}; (iii) the constant phase element of the electric double layer CPE_{dl}; (iv) the resistance of the adsorbed film R_f; and (v) the constant phase element of the adsorbed film CPE_f is shown in Fig. 12b.

In the case of the polished Fe–Mn sample after 1 h of immersion, the results indicate three time constants, which are associated with the characteristics of electric double layer, the surface film and the existence of metastable species during the dissolution of the alloy (Fig. 9). The inductive process was confirmed by a measurement of a positive phase angle in the low-frequency region. In the equivalent circuit applied for the evaluation of the experimental data (Fig. 12c), R_s referred to the solution resistance. The R_{ct} represented the charge-transfer resistance and was coupled with the capacitance of the double layer (CPE_{dl}). The R_f was related to the film resistance and was coupled with the intermediate film capacitance (CPE_f). R_L and L referred to the second adsorbed intermediate process that enhances the

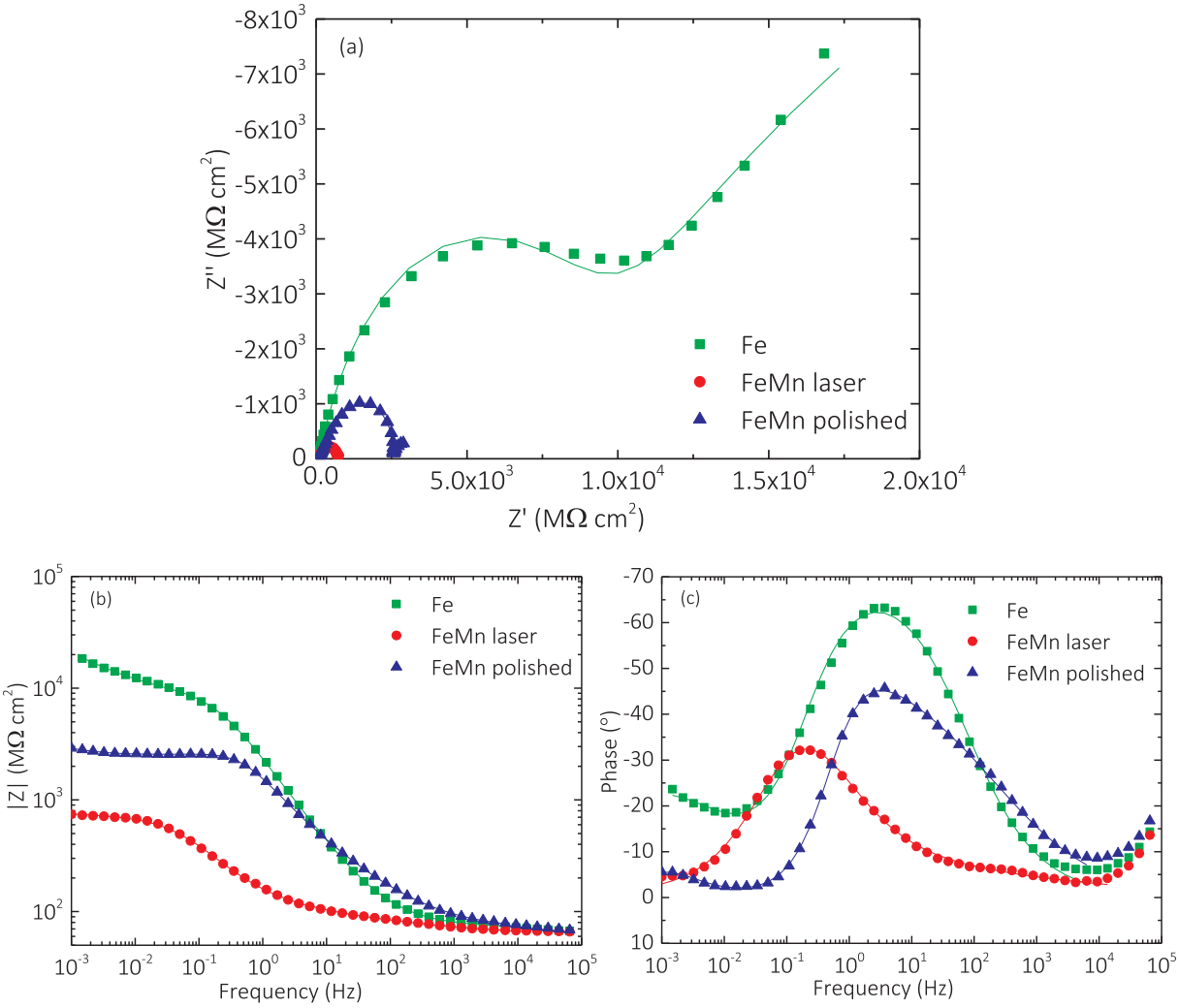

Fig. 11. EIS spectra (a) Nyquist, (b) and (c) Bode–Bode diagrams for Fe, Fe–Mn polished and Fe–Mn laser-textured samples after immersion in Hank's solution for 3 days.

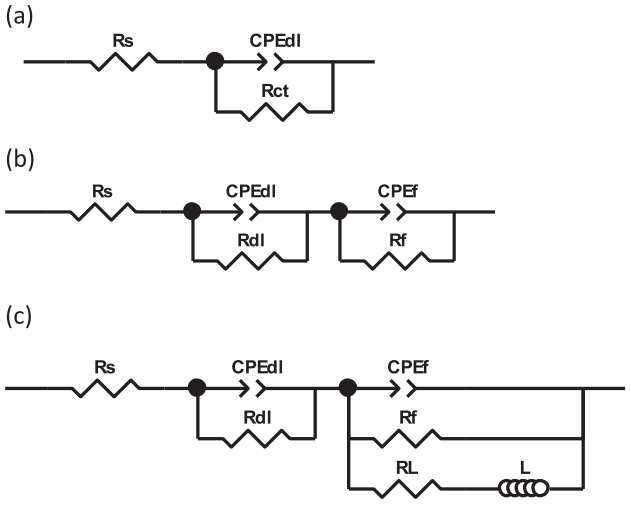

Fig. 12. Equivalent electrical circuits for modelling the EIS data with (a) one time constant, (b) two time constant and (c) three time constant.

electrochemical reaction. After 3–72 h of immersion, the results no longer exhibited a low-frequency inductive process and the spectra were characterized by two time constants, as in the case of the laser-textured Fe–Mn alloy (Figs. 10–12b).

In the case of pure Fe, the spectra were characterized by two time constants, corresponding to the formation of the surface film and to the characteristics of the double layer (Figs. 9–11). The equivalent circuit that was used to fit the experimental data is presented in Fig. 12b.

Magnitude plots revealed that the total impedance for the polished and laser-textured Fe–Mn sample decreased compared to the pure Fe, which indicates the lower corrosion stability of the Fe–Mn alloy, especially after laser texturing. For the laser-textured Fe–Mn sample, the process at lower frequencies dominated the spectrum. It was accompanied by a second process observed as a shoulder near the dominating process after longer immersion times. In the case of the polished Fe–Mn sample and the pure Fe, the dominating process shifted to the medium frequency range. The fitting results are presented in Table 3. The decreased corrosion stability of the Fe–Mn alloy, especially after laser texturing was confirmed, exhibiting decreasing *R* values and higher *CPE* values compared to Fe. The obtained results show a significant improvement in terms of the biodegradability of the Fe–Mn alloy compared to Fe, manifesting in lower *R* values and higher CPE values. Furthermore, the laser texturing provided additionally enhanced biodegradability due to the changes in the surface composition after the laser texturing.

Table 3
Fitting parameters for the laser-textured Fe–Mn alloy, polished Fe–Mn alloy and Fe after 1 h and 72 h of immersion in Hanks solution.

	t/h	$R_{ct}/\Omega\,cm^2$	$CPE_{dl}/\Omega^{-1}\,cm^{-2}\,s^{-n}$	n_1	$R_f/\Omega\,cm^2$	$CPE_f/\Omega^{-1}\,cm^{-2}\,s^{-n}$	n_2	$R_L/\Omega\,cm^2$	L/H cm^{-2}
Fe	1	3368	1.02E−04	0.81	2477	7.12E−03	0.74		
	72	8146	1.03E−04	0.85	47,727	8.54E−04	0.53		
FeMn laser	1	1432	1.12E−02	0.74					
	72	560	4.01E−03	0.77	195	7.13E−03	0.23		
FeMn polished	1	2231	3.14E−04	0.74	964.4	1.47E−04	0.80	1477	1.51E+05
	72	1770	1.33E−04	0.60	879.1	3.28E−04	0.85		

4. Conclusions

In the present study we have shown that the laser texturing of the Fe–Mn alloy significantly increases the corrosion rate due to increased surface area and formation of metal oxides. Moreover, this kind of laser-induced surface functionalization triggers the corrosion that is self-driven by further production of corrosion products leading to biodegradability of the whole sample - although the laser-modified surface is already removed. The XPS analysis revealed that the oxide layer on the laser-textured Fe–Mn alloy consists mainly of Fe_2O_3 and FeO with the content of Mn in the oxide layer significantly higher compared to the bulk. Since laser-surface interaction enable to control this chemical modification, the corrosion rate can be tailored by laser texturing to the desired values. The results of the electrochemical measurements, potentiodynamic and electrochemical impedance spectroscopy, have further confirmed the superior biodegradability of the laser-textured Fe–Mn sample even after the elimination of the textured structure from the surface. The calculated corrosion rate for the laser-textured Fe–Mn samples compared to the polished Fe–Mn is increased by 10-times, which we believe, represents the necessary breakthrough required for using such Fe-based alloys in selected medical applications, especially in orthopaedics.

Acknowledgement

The authors gratefully acknowledge research department on the Institute of Metals and Technology, “Metallic Materials and Technology – Laboratory of Process Metallurgy” and its head dr. Franc Tehovnik for the production of the Fe–Mn alloy. The authors acknowledge the financial support from the Slovenian Research Agency (research core fundings Nos. P2-0132 and P2-0392).

References

[1] J. Hufenbach, F. Kochta, H. Wendrock, A. Voss, L. Giebeler, S. Oswald, S. Pilz, U. Kuehn, A. Lode, M. Gelinsky, A. Gebert, S and B microalloying of biodegradable Fe-30Mn-1C-Effects on microstructure, tensile properties, in vitro degradation and cytotoxicity, Mater. Des. 142 (2018) 22–35, http://dx.doi.org/10.1016/j.matdes.2018.01.005.

[2] S. Ray, U. Thormann, M. Eichelroth, M. Budak, C. Biehl, M. Rupp, U. Sommer, T. El Khassawna, F.I. Alagboso, M. Kampschulte, M. Rohnke, A. Henss, K. Peppler, V. Linke, P. Quadbeck, A. Voigt, F. Stenger, D. Karl, R. Schnettler, C. Heiss, K.S. Lips, V. Alt, Strontium and bisphosphonate coated iron foam scaffolds for osteoporotic fracture defect healing, Biomaterials 157 (2018) 1–16, http://dx.doi.org/10.1016/j.biomaterials.2017.11.049.

[3] R. Drevet, Y. Zhukova, P. Malikova, S. Dubinskiy, A. Korotitskiy, Y. Pustov, S. Prokoshkin, Martensitic transformations and mechanical and corrosion properties of Fe-Mn-Si alloys for biodegradable medical implants, Metall. Mater. Trans. A – Physical Metall. Mater. Sci. 49A (2018) 1006–1013, http://dx.doi.org/10.1007/s11661-017-4458-2.

[4] T. Jurgeleit, E. Quandt, C. Zamponi, Magnetron sputtering as a fabrication method for a biodegradable Fe32Mn alloy, Materials (Basel) 10 (2017), http://dx.doi.org/10.3390/ma10101196.

[5] M. Schinhammer, A.C. Hänzi, J.F. Löffler, P.J. Uggowitzer, Design strategy for biodegradable Fe-based alloys for medical applications, Acta Biomater. 6 (2010) 1705–1713, http://dx.doi.org/10.1016/j.actbio.2009.07.039.

[6] Y. Yun, Z. Dong, N. Lee, Y. Liu, D. Xue, X. Guo, J. Kuhlmann, A. Doepke, H.B. Halsall, W. Heineman, S. Sundaramurthy, M.J. Schulz, Z. Yin, V. Shanov, D. Hurd, P. Nagy, W. Li, C. Fox, Revolutionizing biodegradable metals, Mater. Today 12 (2009) 22–32, http://dx.doi.org/10.1016/S1369-7021(09)70273-1.

[7] Y.P. Feng, A. Blanquer, J. Fornell, H. Zhang, P. Solsona, M.D. Baro, S. Surinach, E. Ibanez, E. Garcia-Lecina, X. Wei, R. Li, L. Barrios, E. Pellicer, C. Nogues, J. Sort, Novel Fe-Mn-Si-Pd alloys: insights into mechanical, magnetic, corrosion resistance and biocompatibility performances, J. Mater. Chem. B 4 (2016) 6402–6412, http://dx.doi.org/10.1039/C6TB01951J.

[8] M. Schinhammer, C.M. Pecnik, F. Rechberger, A.C. Hänzi, J.F. Löffler, P.J. Uggowitzer, Recrystallization behavior, microstructure evolution and mechanical properties of biodegradable Fe–Mn–C(–Pd) TWIP alloys, Acta. Mater. 60 (2012) 2746–2756, http://dx.doi.org/10.1016/j.actamat.2012.01.041.

[9] H. Hermawan, D. Dubé, D. Mantovani, Developments in metallic biodegradable stents, Acta Biomater. 6 (2010) 1693–1697, http://dx.doi.org/10.1016/j.actbio.2009.10.006.

[10] H. Hermawan, H. Alamdari, D. Mantovani, D. Dubé, Iron-manganese: new class of metallic degradable biomaterials prepared by powder metallurgy, Powder. Metall. 51 (2008), http://dx.doi.org/10.1179/174329008X284868.

[11] B. Liu, Y.F. Zheng, Effects of alloying elements (Mn Co, Al, W, Sn, B, C and S) on biodegradability and in vitro biocompatibility of pure iron, Acta Biomater. 7 (2011) 1407–1420, http://dx.doi.org/10.1016/j.actbio.2010.11.001.

[12] W. Lin, L. Qin, H. Qi, D. Zhang, G. Zhang, R. Gao, H. Qiu, Y. Xia, P. Cao, X. Wang, W. Zheng, Long-term in vivo corrosion behavior, biocompatibility and bioresorption mechanism of a bioresorbable nitrided iron scaffold, Acta Biomater. 54 (2017), http://dx.doi.org/10.1016/j.actbio.2017.03.020.

[13] Y.F. Zheng, X.N. Gu, F. Witte, Biodegradable metals, Mater. Sci. Eng. R. Rep. 77 (2014) 1–34, http://dx.doi.org/10.1016/j.mser.2014.01.001.

[14] D. Vojtech, J. Kubasek, J. Capek, I. Pospisilova, Comparative mechanical and corrosion studies on magnesium, zinc and iron alloys as biodegradable metals, Mater. Tehnol. 49 (2015) 877–882.

[15] M. Schinhammer, P. Steiger, F. Moszner, J.F. Löffler, P.J. Uggowitzer, Degradation performance of biodegradable FeMnC(Pd) alloys, Mater. Sci. Eng. C 33 (2013) 1882–1893, http://dx.doi.org/10.1016/j.msec.2012.10.013.

[16] M.P. Staiger, A.M. Pietak, J. Huadmai, G. Dias, Magnesium and its alloys as orthopedic biomaterials: a review, Biomaterials 27 (2006) 1728–1734, http://dx.doi.org/10.1016/j.biomaterials.2005.10.003.

[17] M.M. Saleh, A.H. Touny, M.A. Al-Omair, M.M. Saleh, Biodegradable/biocompatible coated metal implants for orthopedic applications, Biomed. Mater. Eng. 27 (2016) 87–99, http://dx.doi.org/10.3233/BME-161568.

[18] A. Kocijan, I. Paulin, C. Donik, M. Hocevar, K. Zelic, M. Godec, M. Hočevar, K. Zelič, M. Godec, Influence of different production processes on the biodegradability of an FeMn17 alloy, Mater. Tehnol. 50 (2016) 805–811, http://dx.doi.org/10.17222/mit.2016.055.

[19] K. Hashimoto, K. Asami, A. Kawashima, H. Habazaki, E. Akiyama, The role of corrosion-resistant alloying elements in passivity, Corros. Sci. (2007) 42–52, http://dx.doi.org/10.1016/j.corsci.2006.05.003.

[20] A. Kawashima, K. Asami, K. Hashimoto, Effect of manganese on the corrosion behavior of chromium-bearing amorphous metal-metalloid alloys, Sci. Rep. Res. Inst. Tohoku Univ. Ser. A – Phys. Chem Metall. 29 (1981) 276–283.

[21] H. Hermawan, Biodegradable Metals: From Concept to Applications, Springer, Berlin, Heidelberg, 2012, , http://dx.doi.org/10.1007/978-3-642-31170-3.

[22] M. Pogorielov, E. Husak, A. Solodivnik, S. Zhdanov, magnesium-based biodegradable alloys: degradation, application, and alloying elements, Interv. Med. Appl. Sci. 9 (2017) 27–38, http://dx.doi.org/10.1556/1646.9.2017.04.

[23] L.-D. Hou, Z. Li, Y. Pan, M.I. Sabir, Y.-F. Zheng, L. Li, A review on biodegradable materials for cardiovascular stent application, Front. Mater. Sci. 10 (2016), http://dx.doi.org/10.1007/s11706-016-0344-x.

[24] S. Swaminathan, M. Spiegel, Effect of alloy composition on the selective oxidation of ternary Fe-Si-Cr, Fe-Mn-Cr model alloys, Surf. Interface. Anal. 40 (2008) 268–272, http://dx.doi.org/10.1002/sia.2732.

[25] Y.J. Gau, J.K. Wu, The influence of alloying elements on the corrosion behaviour of Fe-Mn-Al alloys, Corros. Prev. Control. 44 (1997) 56–60.

[26] H. Li, Y. Zheng, L. Qin, Progress of biodegradable metals, Prog. Nat. Sci. Mater. Int. 24 (2014) 414–422, http://dx.doi.org/10.1016/j.pnsc.2014.08.014.

[27] M. Zhu, Z. Du, Z. Yin, W. Zhou, Z. Liu, S.H. Tsang, E.H.T. Teo, Low-temperature in situ growth of graphene on metallic substrates and its application in anticorrosion, ACS Appl. Mater. Interfaces 8 (2016) 502–510, http://dx.doi.org/10.1021/acsami.5b09453.

[28] J. Mougin, A. Galerie, M. Dupeux, N. Rosman, G. Lucazeau, A.M. Huntz, L. Antoni, In-situ determination of growth and thermal stresses in chromia scales formed on a ferritic stainless steel, Mater. Corros. Und Korrosion 53 (2002) 486–490.

[29] J. Hufenbach, H. Wendrock, F. Kochta, U. Kühn, A. Gebert, Novel biodegradable Fe-Mn-C-S alloy with superior mechanical and corrosion properties, Mater. Lett. 186 (2017) 330–333, http://dx.doi.org/10.1016/j.matlet.2016.10.037.

[30] J. Zhou, Y. Yang, M. Alonso Frank, R. Detsch, A.R. Boccaccini, S. Virtanen, Accelerated degradation behavior and cytocompatibility of pure iron treated with

sandblasting, ACS Appl. Mater. Interfaces 8 (2016) 26482–26492, http://dx.doi.org/10.1021/acsami.6b07068.
[31] A. Dunn, K.L. Wlodarczyk, J.V. Carstensen, E.B. Hansen, J. Gabzdyl, P.M. Harrison, J.D. Shephard, D.P. Hand, Laser surface texturing for high friction contacts, Appl. Surf. Sci. 357 (2015) 2313–2319, http://dx.doi.org/10.1016/j.apsusc.2015.09.233.
[32] S. Razi, K. Madanipour, M. Mollabashi, Laser surface texturing of 316L stainless steel in air and water: a method for increasing hydrophilicity via direct creation of microstructures, Opt. Laser. Technol. 80 (2016) 237–246, http://dx.doi.org/10.1016/j.optlastec.2015.12.022.
[33] H. Li, Y. Wang, Q. Peng, High degradation rate of Fe-20Mn-based bio-alloys by accumulative cryo-rolling and annealing, Mater. Sci. Eng. C 79 (2017), http://dx.doi.org/10.1016/j.msec.2017.05.004.
[34] L. de lara, R. Jagdheesh, J.L. Ocana, Corrosion resistance of laser patterned ultra-hydrophobic aluminium surface, Mater. Lett. 184 (2016) 100–103, http://dx.doi.org/10.1016/j.matlet.2016.08.022.
[35] U. Trdan, M. Hočevar, P. Gregorčič, Transition from superhydrophilic to super-hydrophobic state of laser textured stainless steel surface and its effect on corrosion resistance, Corros. Sci. (2017), http://dx.doi.org/10.1016/j.corsci.2017.04.005.
[36] P. Gregorcic, B. Setina-Batic, M. Hocevar, Controlling the stainless steel surface wettability by nanosecond direct laser texturing at high fluences, Appl. Phys. A - Mater. Sci. Process. 123 (2017), http://dx.doi.org/10.1007/s00339-017-1392-5.
[37] A.A. Ghoneim, A.M. Fekry, M.A. Ameer, Electrochemical behavior of magnesium alloys as biodegradable materials in Hank's solution, Electrochim. Acta 55 (2010) 6028–6035, http://dx.doi.org/10.1016/j.electacta.2010.05.062.
[38] L.F. Li, M. Daerden, P. Caenen, J.P. Celis, Electrochemical behavior of hot-rolled 304 stainless steel during chemical pickling in HCl-based electrolytes, J. Electrochem. Soc. 153 (2006) B145–B150, http://dx.doi.org/10.1149/1.2177136.
[39] D.R. Baer, M.H. Engelhard, A.S. Lea, P. Nachimuthu, T.C. Droubay, J. Kim, B. Lee, C. Mathews, R.L. Opila, L.V. Saraf, W.F. Stickle, R.M. Wallace, B.S. Wright, Comparison of the sputter rates of oxide films relative to the sputter rate of SiO_2, J. Vac. Sci. Technol. A Vacuum Surfaces 28 (2010) 1060–1072, http://dx.doi.org/10.1116/1.3456123.
[40] A. Zalar, Improved depth resolution by sample rotation during Auger electron spectroscopy depth profiling, Thin. Solid. Films 124 (1985) 223–230 http://www.sciencedirect.com/science/article/B6TW0-46SPM7V-BF/2/449c372a0006514388d2283199a6079d.
[41] C. Palacio, H.J. Mathieu, V. Stambouli, D. Landolt, XPS study of in-situ oxidation of an Fe-Cr alloy by low-pressure oxygen in the presence of water-vapor, Surf. Sci. 295 (1993) 251–262.
[42] E. Paparazzo, On the quantitative XPS analysis of Fe_2O_3 and $Fe_{1-x}O$ oxides, J. Electron. Spectros. Relat. Phenomena 154 (2006) 38–40, http://dx.doi.org/10.1016/j.elspec.2006.09.004.
[43] M. Mullet, V. Khare, C. Ruby, XPS study of Fe(II)-Fe(III) (oxy)hydroxycarbonate green rust compounds, Surf. Interface. Anal. 40 (2008) 323–328, http://dx.doi.org/10.1002/sia.2758.
[44] W. Fredriksson, K. Edstrom, C.A. Olsson, XPS analysis of manganese in stainless steel passive films on 1.4432 and the lean duplex 1.4162, Corros. Sci. 52 (2010) 2505–2510 file:///Users/crtomirdonik/Documents/Papers/2010/Fredriksson/Corros Sci 2010 Fredriksson.pdf.
[45] J.R. Lince, S.V. Didziulis, D.K. Shuh, T.D. Durbin, J.A. Yarmoff, Interaction of O2 with the Fe0.84Cr0.16(001) surface studied by photoelectron-spectroscopy, Surf. Sci. 277 (1992) 43–63.
[46] G.P. Halada, D. Kim, C.R. Clayton, Influence of nitrogen on electrochemical passivation of high-nickel stainless steels and thin molybdenum-nickel films, Corros. sci. 52 (1996) 36–46.
[47] E.M. Westin, C.O.A. Olsson, S. Hertzman, Weld oxide formation on lean duplex stainless steel, Corros. Sci. 50 (2008) 2620–2634, http://dx.doi.org/10.1016/j.corsci.2008.06.024.
[48] P.J. Cumpson, The Thickogram: a method for easy film thickness measurement in XPS, Surf. Interface Anal. 29 (2000) 403–406.
[49] C. Donik, A. Kocijan, D. Mandrino, I. Paulin, M. Jenko, B. Pihlar, Initial oxidation of duplex stainless steel, Appl. Surf. Sci. 255 (2009) 7056–7061, http://dx.doi.org/10.1016/j.apsusc.2009.03.041.
[50] L.L. Shreir, G.T. Burstein, R.A. Jarman, Corrosion, Butterworth-Heinemann, 1994 https://www.sciencedirect.com/science/book/9780080523514 (accessed March 15, 2018).
[51] A.-M. Kietzig, S.G. Hatzikiriakos, P. Englezos, Patterned superhydrophobic metallic surfaces, Langmuir 25 (2009) 4821–4827, http://dx.doi.org/10.1021/la8037582.
[52] D.V. Ta, A. Dunn, T.J. Wasley, R.W. Kay, J. Stringer, P.J. Smith, C. Connaughton, J.D. Shephard, Nanosecond laser textured superhydrophobic metallic surfaces and their chemical sensing applications, Appl. Surf. Sci. 357 (2015) 248–254, http://dx.doi.org/10.1016/j.apsusc.2015.09.027.
[53] G. McHale, N.J. Shirtcliffe, M.I. Newton, Super-hydrophobic and super-wetting surfaces: analytical potential? Analyst 129 (2004) 284–287, http://dx.doi.org/10.1039/b400567h.